

Radiation damage of water in environmental scanning electron microscopy

C. P. ROYALL, B. L. THIEL AND A. M. DONALD

Polymers and Colloids Group, Cavendish Laboratory, Department of Physics, University of Cambridge, Madingley Road, Cambridge, CB3 0HE, U.K.

Key words. Beam damage, environmental SEM, ESEM, free radical, hydrated samples, radiolysis, water.

Summary

Specimen damage from the electron beam poses a considerable problem with electron microscopy. This damage is particularly acute in environmental scanning electron microscopy (ESEM) for two reasons. Firstly, owing to its ability to stabilise insulating and hydrated specimens, ESEM lends itself to polymeric and biological materials that are typically highly beam-sensitive. Secondly, water acts as a source of small, highly mobile free radicals, which accelerate specimen degradation.

By taking the results of single-particle simulations of electron–water interactions, we determine the concentration of reactive species in a water specimen under ESEM conditions. We consider 12 species, which are produced in a Gaussian distribution, and annihilate according to a second-order reaction scheme. Self-diffusion along the concentration gradient is also modelled.

We find that the dominant reactive species is the hydroxyl (.OH) radical. Annihilation of this species is suppressed due to the lower concentration of reactants. The relatively stable hydrogen peroxide is also found at large concentrations. By comparing two beam energies, 5 and 25 keV, we find a drastic increase in the quantities of reactive species produced with beam energy. The longer range of 25 keV primary electrons spreads reactive species over a wider region, which then decay far more slowly.

Introduction

Electron microscopy of ‘soft’ materials is limited by structural and compositional damage from the electron beam. The information extracted from the specimen is thus limited by the maximum electron dose that can be tolerated. This radiation damage can severely restrict the effective resolution, as the dose increases with the square of the magnification. Different materials show widely varying

susceptibility to the electron beam. Metals show little damage, but saturated polymers can be very sensitive indeed (Talmon, 1987).

Environmental scanning electron microscopy (ESEM) is unique in enabling the imaging of hydrated specimens (Danilatos, 1993). This allows a number of novel *in-situ* experiments to be carried out, along with the study of materials entirely inaccessible to other forms of electron microscopy (Thiel & Donald, 1998).

The presence of liquid water is known to increase radiation damage in ESEM (Jenkins & Donald, 1997; Kitching & Donald, 1998). Radiation damage to hydrated specimens can be minimized by adjusting the operating parameters, such as beam energy. This has been done for polypropylene (Kitching & Donald, 1998). At a more fundamental level, the electron beam–specimen system can be modelled numerically, to gain an improved understanding of beam damage, which is the approach followed here. This can lead to the study of systems that are intrinsically less beam-sensitive, and to simplify the minimization of beam damage.

The passage of the high-energy primary electrons (PE) from the beam imparts energy to the specimen through ionization, excitation and displacement. The excited or ionized molecules may then undergo further ionization or bond scission in the case of polymeric or biological specimens. Chain scission in polymers alters the molecular weight, and the smaller molecules produced may evaporate reducing the mass of the specimen. The free radicals produced by ionization and bond scission can then attack the specimen (Talmon, 1987).

Radiation damage involving water has been studied for conventional SEM. Biological specimens are frozen, and imaged at liquid nitrogen temperatures in cryo-SEM. Under irradiation, ice acts as a source of small, highly mobile free radicals, which provide more mechanisms for radiation damage (Talmon, 1987). Water in ESEM should behave in a similar way, only here the mobility of reactive species is

increased substantially in the liquid medium. As a simplest case for a hydrated specimen, pure water is considered here.

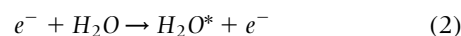
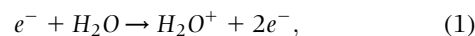
Electron–water interactions have been studied extensively through simulations (La Verne & Mozumder, 1983; Terrissol & Beaudre, 1990; Pimblott *et al.*, 1991; Hill & Smith, 1994; Pimblott *et al.*, 1996) and experimental work (Jonah *et al.*, 1976; Jonah & Miller, 1977). This has enabled the free radical and ionic products to be quantified in the case of a single PE. The results of the simulations can be applied to ESEM conditions, where instead of a single incident electron there is an electron beam. The number of reactive species is too large for individual particles to be considered, so instead an averaging approach is used to find their concentration. This is expected to determine the dominant damage-causing species produced in water, and also their mobility.

This work begins with a review of electron–water interactions, at the single-particle level. The application of these to ESEM conditions, with a many-electron beam is discussed, with particular attention paid to approximations made. We consider ESEM conditions to be a 5 nA beam (Fletcher, 1998) and compare the effects of beam energies of 5 and 25 keV, representing typical limits of ESEM operation. Next, the model used in the work is constructed and the main results are presented. It is worth pointing out at this stage that the object of this work is not to provide a highly accurate description of the system on the atomic level, but rather to determine the main damage mechanisms and identify how these may be minimized. Note that although water is frequently present as a vapour above the specimen in ESEM, here liquid water within the specimen is considered. This water vapour also produces an electron skirt (Danilatos, 1993) of PEs scattered out of the main beam. Although under certain experimental conditions (long beam path through the gas and high pressure) a considerable number of PEs can be scattered out of the primary beam, the impact on the specimen is expected to be rather small. The electrons are scattered over a wide area (~500 μm radius) and are therefore expected to produce only very low concentrations of reactive species. The major effect is to reduce the primary beam current at the point of impact. However, the 5 nA current modelled is only a nominal value, so the contribution from the primary beam skirt is neglected.

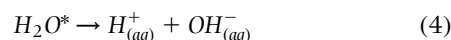
Electron–water interactions

The passage of high-energy electrons through water has been studied through simulations involving one PE. This electron undergoes a number of inelastic scattering events by which it imparts energy to the water medium, and is eventually absorbed, after it has lost sufficient energy (Hill & Smith, 1994).

The inelastic scattering events result in ionization or excitation of the water molecules,



These excited state water molecules may then decay into free radicals or ions, for example,



where the dots represent unpaired electrons (Talmon, 1987).

Each inelastic scattering event produces typically six reactive species in a space of a few nanometres (Hill & Smith, 1994). These regions containing reactive species are termed spurs. For electrons with energy of the order of 5–25 keV, the average distance between these spurs (the mean free path) is large compared to their size (Table 1) (La Verne & Mozumder, 1983).

The reactive species then either recombine in annihilation reactions (Table 2) or diffuse away from the spur, where they are relatively unlikely to annihilate. Of course, reaction with water is possible (Table 2), but this simply produces more reactive species. Decay within the spur takes place on a timescale of 10^{-10} to 10^{-9} s (Hill & Smith, 1994). Those species that have not recombined at this time are termed the primary yield (Table 3) (Terrissol & Beaudre, 1990). The whole process is termed radiolysis.

From one electron to a beam

The essential task in this work is to apply the results for a single PE to a beam. Treating each PE and all its products

Table 1. Parameters used for 5 and 25 keV primary electrons.

PE energy (keV)	Mean free path λ_{PE} (nm)	Mean range $\langle R \rangle$ (μm)	Normalization constant $2A$ ($\text{M dm}^{-3}\text{s}^{-1}$)	$\frac{\partial}{\partial t} \Phi_{\alpha}(0, t)$
5	15*	0.461**	1.29×10^{15}	67.15
25	55*	7.0**	3.70×10^{11}	0.00191

*From Hill & Smith (1994), ** from La Verne & Mozumder (1983)

Table 2 Reactions and rate constants used by Hill & Smith (1994). The final products are water, hydrogen peroxide and hydrogen gas

Reaction	Rate constant $\times 10^{10} \text{ M}^{-1} \text{ s}^{-1}$
(1) $2\cdot\text{OH} \rightarrow \text{H}_2\text{O}_2$	0.45
(2) $2e_{(\text{aq})}^- \rightarrow \text{H}_2 + 2\text{OH}_{(\text{aq})}^-$	0.5
(3) $2\cdot\text{H} \rightarrow \text{H}_2$	2.0
(4) $\cdot\text{OH} + e_{(\text{aq})}^- \rightarrow \text{OH}_{(\text{aq})}^-$	3.0
(5) $\cdot\text{H} + \cdot\text{OH} \rightarrow \text{H}_2\text{O}$	2.0
(6) $\text{H}_{(\text{aq})}^+ + \text{OH}_{(\text{aq})}^- \rightarrow \text{H}_2\text{O}$	14.3
(7) $\cdot\text{H} + \text{H}_2\text{O}_2 \rightarrow \text{H}_2\text{O} + \cdot\text{OH}$	0.016
(8) $e_{(\text{aq})}^- + \text{H}_{(\text{aq})}^+ \rightarrow \cdot\text{H}$	2.3
(9) $e_{(\text{aq})}^- + \cdot\text{H} \rightarrow \text{H}_2 + \text{OH}_{(\text{aq})}^-$	2.5
(10) $\text{H}_2\text{O}_2 + e_{(\text{aq})}^- \rightarrow \text{OH}_{(\text{aq})}^- + \cdot\text{OH}$	1.2
(11) $e_{(\text{aq})}^- + \text{O}_2 \rightarrow \text{O}_2^-$	1.9
(12) $e_{(\text{aq})}^- + \text{O}_2^- \rightarrow \text{OH}_{(\text{aq})}^- + \text{HO}_2^-$	1.3
(13) $e_{(\text{aq})}^- + \cdot\text{HO}_2 \rightarrow \text{HO}_2^-$	2.0
(14) $\cdot\text{H} + \text{O}_2 \rightarrow \text{HO}_2$	1.9
(15) $\cdot\text{H} + \text{O}_2^- \rightarrow \text{HO}_2^-$	2.0
(16) $\cdot\text{H} + \text{HO}_2 \rightarrow \text{H}_2\text{O}_2$	2.0
(17) $\text{H}_{(\text{aq})}^+ + \text{O}_2^- \rightarrow \text{HO}_2$	5.0
(18) $\cdot\text{OH} + \text{O}_2^- \rightarrow \text{OH}_{(\text{aq})}^- + \text{O}_2$	1.2
(19) $\cdot\text{OH} + \text{HO}_2 \rightarrow \text{H}_2\text{O} + \text{O}_2$	1.2
(20) $\cdot\text{OH} + \text{OH}_{(\text{aq})}^- \rightarrow \text{H}_2\text{O} + \cdot\text{O}^-$	1.3
(21) $\cdot\text{H} + \text{OH}_{(\text{aq})}^- \rightarrow \text{H}_2\text{O} + e_{(\text{aq})}^-$	0.0021
(22) $\cdot\text{OH} + \text{HO}_2 \rightarrow \text{O}_2 + \text{H}_2\text{O}$	0.0033
(23) $\cdot\text{OH} + \cdot\text{O}^- \rightarrow \text{HO}_2^-$	1.8
(24) $\cdot\text{OH} + \text{HO}_2^- \rightarrow \text{O}_2^-$	0.75
(25) $e_{(\text{aq})}^- + \text{HO}_2^- \rightarrow 2\text{OH}_{(\text{aq})}^- + \text{H}_2$	0.35
(26) $e_{(\text{aq})}^- + \text{O}^- \rightarrow 2\text{OH}_{(\text{aq})}^-$	2.2
(27) $\cdot\text{H} + \cdot\text{O}^- \rightarrow \text{OH}_{(\text{aq})}^-$	2.0
(28) $\text{H}_{(\text{aq})}^+ + \cdot\text{O}^- \rightarrow \cdot\text{OH}$	5.0
(29) $\text{H}_{(\text{aq})}^+ + \text{HO}_2^- \rightarrow \text{H}_2\text{O}_2$	5.0

individually is not practical, so some averaging approach is desirable.

Here we discuss the differences between the single PE and beam, and how they may be treated. We want to obtain a concentration of each species. As will be seen later, this is straightforward to determine. Furthermore, we will seek to model the creation of reactive species as a smooth analytic function, giving concentrations as formed by radiolysis. This section will argue that each species may be treated by an average concentration, and that the spatial distribution in which they are formed is approximately Gaussian.

A continuous concentration

In the case of a single PE, following spur decay, the residual reactive species are isolated, as they have diffused away from the spurs into the bulk water. In this case, we expect the concentrations to become uniform eventually, and that

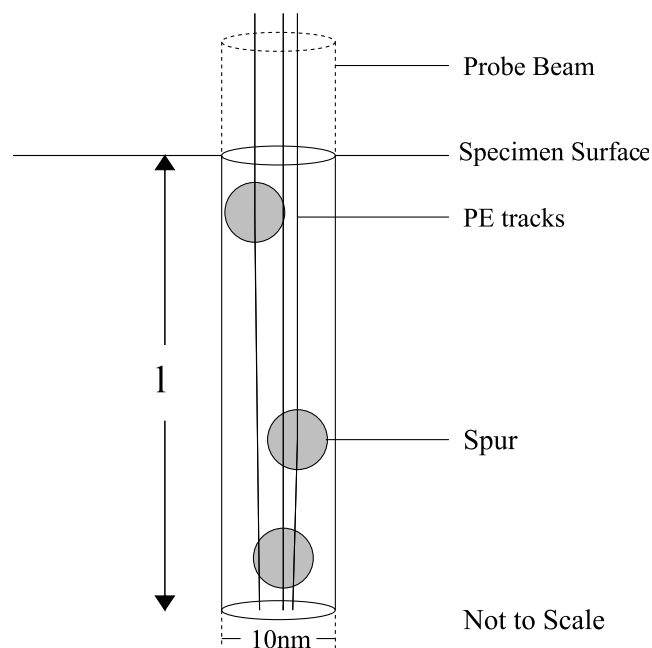


Fig. 1. Close to the surface, the angular scattering of primary electrons is sufficiently small to be neglected, so the interaction volume may be modelled as a cylinder (not to scale). A calculation of spur overlap may be made by assuming that each incident electron (bold line) produces one spur (grey circle) within its mean free path.

the primary yields are a good starting point for further evolution.

The spurs are of finite size and separation; if enough PEs are incident on the specimen, we expect the spurs to overlap. That is, two or more elastic scattering events occur sufficiently close together that reactive species from different events can annihilate with each other. In this case, we expect a more complete annihilation than in the single PE case. Those species diffusing beyond the spur in which they were formed simply enter another spur in which to react. This contrasts with the reactive species produced by the single PE diffusing around the bulk, which are unlikely to find annihilation partners. In order for the primary yields to be valid, we need to show that spur overlap is not present, or at least not significant.

The highest beam current for imaging in ESEM is typically 5 nA (Fletcher, 1997), although this can be significantly higher during microanalysis. The time scale of spur decay is 10^{-10} to 10^{-9} s, and during this time between three and 30 additional PEs arrive. In order to crudely determine spur overlap, we calculate the volume occupied by the spurs as a fraction of the total volume in the most irradiated region of the specimen.

Clearly the most irradiated region is that directly below the electron beam. Because forward scattering dominates at the energies considered (Hill & Smith, 1994), we can model

this region as a cylinder, whose width is equal to that of the electron beam, which is of order 10 nm (Goldstein *et al.*, 1992), as shown in Fig. 1. The height of the cylinder is the length in which we expect one scattering event to occur, i.e. the mean free path.

The mean free path is determined from

$$\lambda_{PE} = \frac{1}{\sigma n_T} \quad (5)$$

where σ is the scattering cross-section (taken from Hill & Smith, 1994) and n_T is the number density of scattering targets. Each spur is assumed to be a sphere of radius 3 nm, whose centre is located within the cylinder. This is consistent with the literature, which typically assumes a few nanometres (Hill & Smith, 1994) (La Verne & Mozumder, 1983). The volume of the cylinder shown in Fig. 1 is equal to approximately 27 and 98 spur volumes for 5 and 25 keV PEs, respectively. These figures suggest some spur overlap, although it is not expected to be dominant. At greater depths, cumulative angular scattering removes PEs from the axial direction, so a treatment assuming no spur overlap is expected to be reasonable to first order. From this discussion we see that using primary yields (Table 3) is appropriate for the level of this work.

The Gaussian interaction volume

The interaction volume is the region of the specimen penetrated by the PE (Goldstein *et al.*, 1992). As mentioned above, PEs scatter away from the initial trajectory, and a teardrop-shaped region is formed (La Verne & Mozumder, 1983; Goldstein *et al.*, 1992). Thus, further into the specimen the motion becomes more isotropic and tends

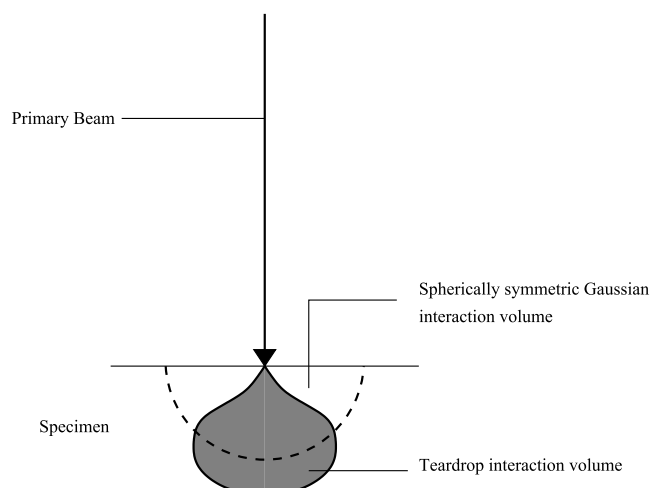


Fig. 2. The difference between the Gaussian interaction volume used here and the teardrop-shaped interaction volume. Although the Gaussian interaction volume is significantly different in shape, its spherical symmetry simplifies the problem.

towards a random walk. In fact the variation in mean PE range between the axial and other directions is only a factor of 0.03 (La Verne & Mozumder, 1983). For a Gaussian distribution, we expect no preferred direction. As the axial direction is only slightly favoured, a treatment based on a spherical Gaussian distribution is indeed appropriate for the level of this work. The Gaussian distribution is centred on the point of contact between the specimen and primary beam, as shown in Fig. 2.

Of course the hemisphere lying above the specimen surface is not part of the interaction volume, so we only treat the hemisphere below the surface, and normalize accordingly by a factor of two. The standard deviation of this Gaussian is then the mean PE range, $\langle R \rangle$, as determined by La Verne & Mozumder (1983) (Table 1). This introduction of spherical symmetry allows a vastly simpler one-dimensional approach to be followed.

Now the assumptions leading to no spur overlap, and a spherical Gaussian distribution around the beam might appear to be based on differing premises. The argument for no spur overlap rests on the assumption that angular scattering is small. Thus, the PEs travel in a straight line, whereas the Gaussian interaction volume requires isotropic motion. These assumptions are reconciled by noting that the argument for no spur overlap concerned only the first few mean free paths of the PE trajectory. Following some inelastic scattering events, the PEs lose energy, and at lower energies, angular scattering is rather more favoured (Hill & Smith, 1994). Furthermore, the number of collisions is sufficiently large (typically in the order of 1000) such that, although the typical scattering angle in each collision is relatively small, on aggregate the PEs move in a reasonably isotropic fashion.

Mean concentration model

Having discussed our assumptions, we now construct a model to describe the system, based on mean concentrations. The concentration profile of each species is produced in a Gaussian distribution, and normalized as shown below. Further radiolysis increases the concentration, which is evolved by the annihilation rate reactions listed in Table 2. Concentration-driven diffusion is also employed to investigate the spread of reactive species beyond the interaction volume.

The concentration of each species α is a function of time t and position \mathbf{r} , $\Phi_\alpha(\mathbf{r}, t)$. Spherical symmetry means that \mathbf{r} can be treated as a scalar, so the concentration is written $\Phi_\alpha(r, t)$.

In order to determine the change in concentration produced by the primary beam, we take the Gaussian envelope of the interaction volume,

$$A \int_0^\pi \int_0^{2\pi} \int_0^\infty \exp\left(-\frac{r^2}{2\langle R^2 \rangle}\right) r^2 dr \sin\theta d\theta d\varphi = 1, \quad (6)$$

with the normalization constant

$$A = \frac{1}{\{\langle R \rangle (2\pi)^{1/2}\}^3}. \quad (7)$$

This is doubled to take account of the fact that we only consider the hemisphere beneath the specimen surface.

The molar rate of PE absorption is the beam current, divided by the electronic charge and Avogadro's number, normalized at $r = 0$ by $2A$.

$$\frac{\partial}{\partial t_{beam}} \Phi_{\alpha}(0, t) = 2A \frac{I_{beam}}{eN_a}, \quad (8)$$

where I_{beam} is the beam current, e is the electronic charge and N_a is Avogadro's number. This is then multiplied by the Gaussian envelope to obtain the molar rate of PE absorption as a function of r ,

$$\frac{\partial}{\partial t_{beam}} \Phi_{\alpha}(r, t) = 2A \frac{I_{beam}}{eN_a} \exp\left(-\frac{r^2}{\langle R^2 \rangle}\right). \quad (9)$$

In order to obtain values for other species, we take the G-values listed in Table 3. As these give the yield per 100 eV absorbed, we multiply by 50 and 250 for 5 and 25 keV, respectively. This then yields the concentration increase with respect to time. There is considerable discrepancy in the literature concerning G-values. Those used here were obtained by Terrissol & Beaudre (1990) because they were calculated for a PE energy of 10 keV, which is within the range used here, except for HO₂ which was obtained from Hill and Smith. The scheme of Hill & Smith (1994) is used to calculate the annihilation reactions (Table 2). The reactions are all assumed to be first order in each reactant,

$$\frac{\partial}{\partial t_{react}} \Phi_{\alpha}(r, t) = -k\Phi_{\alpha}(r, t)\Phi_{\beta}(r, t), \quad (10)$$

where k is the rate constant (Table 1). The evolution of the $\Phi_{\alpha}(r, t)$ are advanced according to the reactions listed in Table 2. A fourth-order Runge–Kutta method for iterative integration of differential equations is used to find the change in concentration at each timestep (Press *et al.*, 1988).

Diffusion

The concentration of the initial yield is not uniform, so species diffuse according to the diffusion equation,

$$\frac{\partial}{\partial t_{diff}} \Phi_{\alpha}(r, t) = -D\nabla^2 \Phi_{\alpha}(r, t), \quad (11)$$

where D is the coefficient of diffusion taken from Table 4 (Reif, 1965). As the system is spherically symmetric, we only need the $\Phi_{\alpha}(r, t)$ in one dimension. From the central difference formula (Kreyszig, 1993), we can obtain the following expression for $D\nabla^2 \Phi_{\alpha}(r, t)$, where the $\Phi_{\alpha}(r, t)$ are defined on an axis passing through the origin of a

Table 3. G-values for the primary yield. The G-value is the number of species produced per 100 eV of energy absorbed. Those used were obtained by Terrissol & Beaudre, for a PE energy of 10 keV. *Denotes values obtained for PE energy = 1 MeV by Hill & Smith (1994).

Ge(aq)	GH	GOH	GH + (aq)	GOH-(aq)	GH2O2	GHO2
2.0	0.8	1.6	2.6	0.6	1.4	0.11*

spherically symmetric system:

$$\begin{aligned} \frac{\partial}{\partial t_{diff}} \Phi_{\alpha}(r, t) \approx & -\frac{D}{h^2} [\Phi_{\alpha}((n-1)h, 0, 0) - 2\Phi_{\alpha}(nh, 0, 0) \\ & + \Phi_{\alpha}((n+1)h, 0, 0)] \\ & - 2\frac{D}{h^2} \{\Phi_{\alpha}((n+1)h, 0, 0) \\ & - \Phi_{\alpha}((n-1)h, 0, 0)\} \left\{ \sqrt{n^2 + 1} - n \right\}, \quad (12) \end{aligned}$$

for the n th element where h is the spatial stepsize such that $r = nh$. Details of the derivation are given in the Appendix. The boundary conditions are chosen such that the origin is treated as a mirror through which there is no net diffusion, and at large values of r the concentration tends towards its equilibrium value (see Appendix).

The change in concentration is then found by

$$\begin{aligned} \frac{\partial}{\partial t_{total}} \Phi_{\alpha}(r, t) = & \frac{\partial}{\partial t_{beam}} \Phi_{\alpha}(r, t) + \frac{\partial}{\partial t_{react}} \Phi_{\alpha}(r, t) \\ & + \frac{\partial}{\partial t_{diff}} \Phi_{\alpha}(r, t), \quad (13) \end{aligned}$$

which is numerically integrated to give $\Phi_{\alpha}(r, t)$. The length of the timestep used is 10^{-9} s.

Table 4 Diffusion constants (Hill & Smith, 1994)

Species	Diffusion coefficient $\times 10^{-5} \text{ cm}^2 \text{ s}^{-1}$
$e^-_{(aq)}$	4.5
$H^+_{(aq)}$	9.0
.H	7.0
.OH	2.8
$OH^-_{(aq)}$	5.0
O^-	2.1
O_2^-	2.1
.O	2.8
H_2O_2	1.4
HO_2^-	1.4
HO_2	2.0

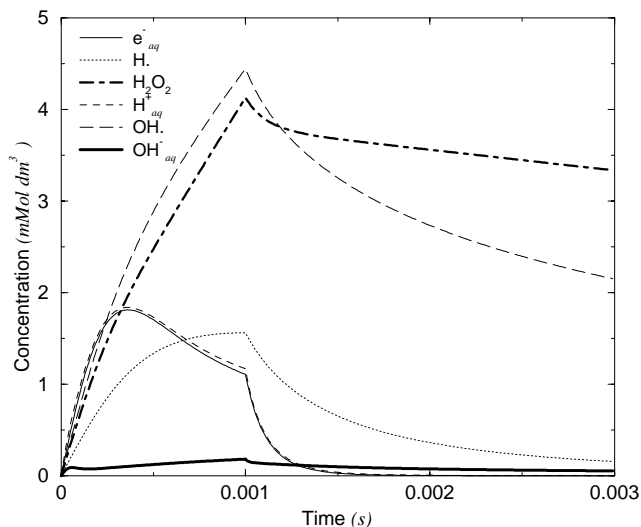


Fig. 3. Generic behaviour of the system, showing peaks for more reactive species, and continuous increase in H_2O_2 and OH^- . 25 keV, dwelltime = 10^{-3} s.

The time for which a particular region of the specimen is irradiated is the *dwelltime*, t_d . This is dependent upon the area scanned (magnification), scan rate and the size of the interaction volume (beam energy). Typical dwelltimes for ESEM are in the range 10^{-6} to 10^{-2} s, which are considered here. A calculation following Eq. (13) is carried out where

$$\frac{\partial}{\partial t_{\text{beam}}} \phi_{\alpha}(r, t)$$

is set to 0 for values of $t > t_d$, and the system is allowed to relax. The dwelltime is varied to simulate different imaging conditions.

Results and discussion

It is possible to present the results of this work in a variety of ways. Six dominant species are considered at two beam energies, for a variety of dwelltimes. An overview is presented before attention is given to the effects of dwelltime, beam energy and particular species.

We begin by discussing the generic behaviour for a 25 keV beam with a moderate dwelltime of 10^{-3} s. At the point where the probe meets the specimen ($r = 0$ for the spherical Gaussian), the maximum rate of creation is found (Eq. (9)). The time evolution is shown in Fig. 3. As can be seen, the species evolve differently, but all decay for times greater than the dwelltime, as the system relaxes. More reactive species – the hydrated electron, hydrogen ion and hydrogen radical – exhibit a peak concentration prior to the end of the dwelltime. Others, such as the hydroxyl radical and hydrogen peroxide only decay once irradiation ceases.

These peaks are due to competition between annihilation

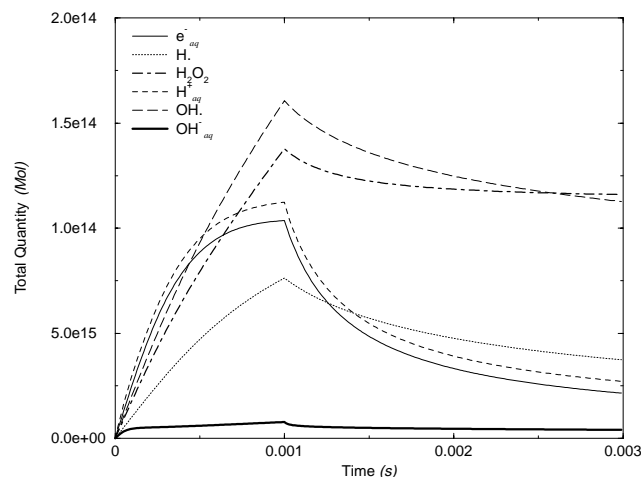


Fig. 4. The total quantities show similar behaviour to central concentrations (Fig. 3), although the timescale is rather longer for the same dwelltime in each system. 25 keV, dwelltime = 10^{-3} s.

reactions, diffusion and creation. Initially, the concentrations are very small, so annihilation is negligible and creation dominates. After a certain time, the concentration is sufficient that the effects of annihilation and diffusion exceed creation. At this point, the concentration begins to fall. The time at which this happens depends on the particular species and beam energy.

The concentrations can be integrated throughout the system, so that an overall picture of total quantity can be built up. Figure 4 shows the same beam energy and dwelltime as that in Fig. 3. Comparison between the two shows a similar overall behaviour; however, the total quantity plot (Fig. 4) has a somewhat broader time-evolution. This can be explained in terms of regions far from the centre. Fewer reactive species are

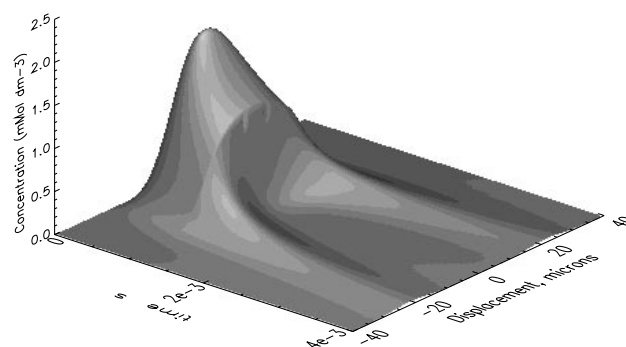


Fig. 5. Time-evolution of the lateral profile of $e_{(aq)}^-$, 25 keV, dwelltime = 10^{-3} s. Note the rapid decay in the centre, and much slower decay at low concentrations.

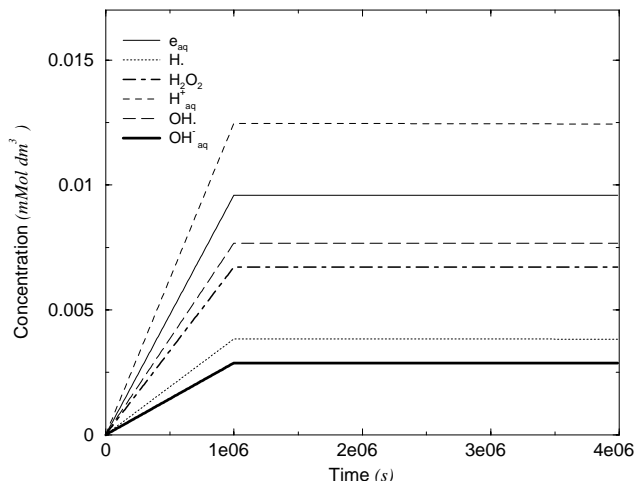


Fig. 6. Early stages of radiolysis: all species increase linearly with time, in accordance with their G -values (Table 3). 25 keV, dwelltime = 10^{-6} s.

produced here, and as the annihilation reactions are second order (Eq. (10)), they are relatively less efficient. This means that it takes longer for the rate of annihilation to exceed creation (neglecting the effects of diffusion). Hence, the broadening and delay of the concentration maxima are not surprising. Further evidence can be seen from the rate of decay. The total quantity decays rather slowly, because the annihilation rate decreases away from the centre.

This is further demonstrated in Fig. 5, a plot of the concentration profile of the hydrated electron, for the same dwelltime and beam energy (10^{-3} s and 25 keV). Here we see that after irradiation ceases, the concentration falls to zero, except at the edges, where two 'horns' have evolved. These represent very slow decay due to low concentrations.

Short dwelltimes

It has already been noted that at short dwelltimes concentration is dominated by creation, so it increases linearly with time. In other words, the contribution from the second and third terms in Eq. (13) can be neglected. This is shown to be true in the case of Fig. 6, for a dwelltime of 10^{-6} s, for 25 keV. The concentration of every species increases linearly with time, in proportion to its G -value, for times less than the dwelltime. After irradiation, there is negligible decay, as can be seen from the flat lines in Fig. 6.

Beam energy

For the same dwelltime as Fig. 3, the 5 keV system shows a markedly different behaviour. The concentrations of all species except hydrogen peroxide and the hydroxyl radical are small (Fig. 7). Longer dwelltimes are further discussed in a subsequent section. Suffice to say, the 5 keV system evolves

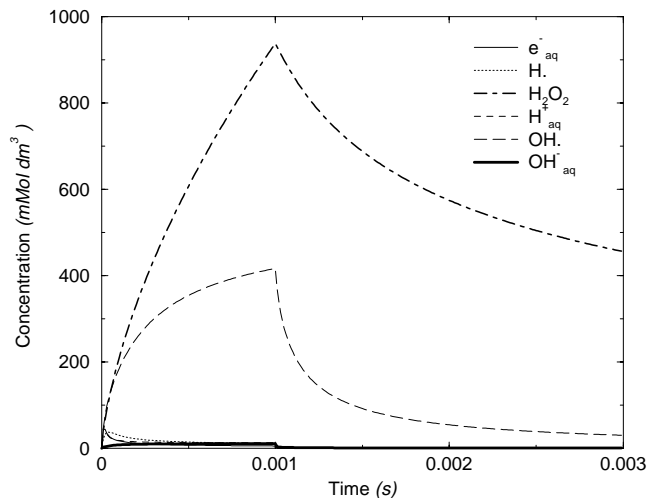


Fig. 7. For the same dwelltime as Fig. 3 (10^{-4} s), the 5 keV system appears markedly different. Central concentrations are dominated by $\cdot OH$ and H_2O_2 , the 5 keV system exhibits the same general behaviour as the 25 keV system.

at a much faster rate than 25 keV, which is demonstrated in Figs 8(a) and (b). These plots show similar generic behaviour to Figs 3 and 4. The peaks for $e_{(aq)}^-$, H and $H^+_{(aq)}$ are again apparent, along with higher concentrations of H_2O_2 and $\cdot OH$. Apart from the dwelltime, there are two main differences:

1 the central concentrations at 5 keV are around 50 times higher.

2 total quantities produced are far higher in the 25 keV case.

In fact, all these effects are the consequences of the main difference between the 5 and 25 keV systems. The mean PE range $\langle R \rangle$ is around 15 times greater for 25 keV PEs (Table 1). This means that the interaction volume is 3400 times larger in the 25 keV case, as it increases as $\langle R \rangle^3$. Thus, the primary yield is spread over a far greater volume, and the concentrations are far lower for 25 keV. However, this is offset to some extent because five times as many species are created overall from the increased energy deposition. The increased concentrations at 5 keV are then a direct result of the shorter mean PE range, as shown in Figs 3 and 8(a).

The concentrations at 5 keV are very much higher when we consider the fact that the dwelltime is only a tenth of the 25 keV dwelltime in Fig. 3. However when scanning a specimen, the dwelltime is related to the time taken for the beam to pass across the interaction volume. As the 25 keV interaction volume is 15 times as wide (Table 1), we expect much longer dwelltimes in this case.

A low concentration regime also means that it takes far longer for annihilation and diffusion to exceed creation, as we have already noted above. That annihilation is effectively suppressed for 25 keV means that the total quantities produced are far greater, and the concentrations peak far later. The effect of the reduction in mean PE range is

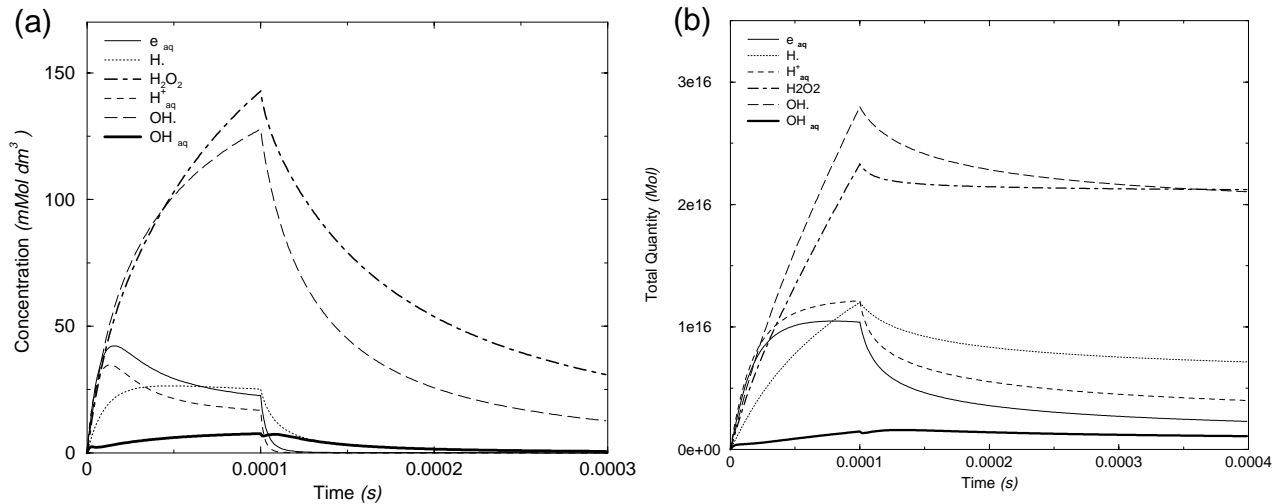


Fig. 8. The 5 keV system exhibits the same general behaviour as the 25 keV system, if the dwelltime is reduced by an order of magnitude. Central concentrations (a) and total quantities (b), both for a dwelltime of 10^{-4} s.

extreme indeed. Excepting the central region, we expect the 25 keV environment to be far more hostile.

Diffusion

It is not easy to decouple the effects of diffusion and annihilation. Both tend to reduce regions of high concentration with respect to those of low concentration. However, we can solve Eq. (13) without a contribution from diffusion for comparison. Figure 9 shows radial concentration profiles for 5 and 25 keV after 10^{-4} s of irradiation.

The central concentration of $\cdot OH$ and $e_{(aq)}$ has fallen by a factor of two as a consequence of diffusion in the 5 keV case

(Fig. 9(a)). There is only a small reduction in central concentration from diffusion in the 25 keV case (Fig. 9(b)). Furthermore, we see that the $e_{(aq)}$ is the most abundant species for 25 keV. The hydrated electron is produced at a greater rate than other species shown; the fact that it remains the most abundant at this time suggests that annihilation reactions are not yet significant, and that the system is still in the range of linear increase with time (Fig. 6). The apparent increase in $e_{(aq)}$ concentration in the diffusing system (Fig. 9(a)) is taken to be a result of increased rates of reaction caused higher concentrations of other species (e.g. $\cdot H$ and $\cdot OH$).

The variation here also stems largely from the different system sizes in each case. The 5 keV system has concentrations

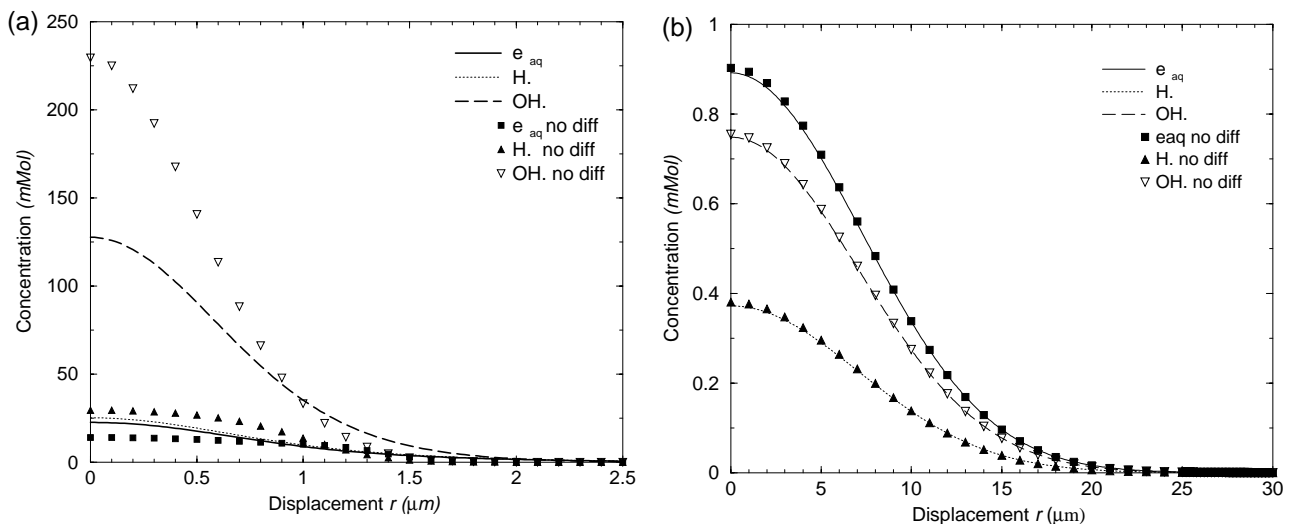


Fig. 9. Radial concentration profiles after a dwelltime of 10^{-4} s (5 keV (a), 25 keV (b)). The thicker lines represent simulations without diffusion. $r = 0$ is the point of contact between the electron beam and the specimen.

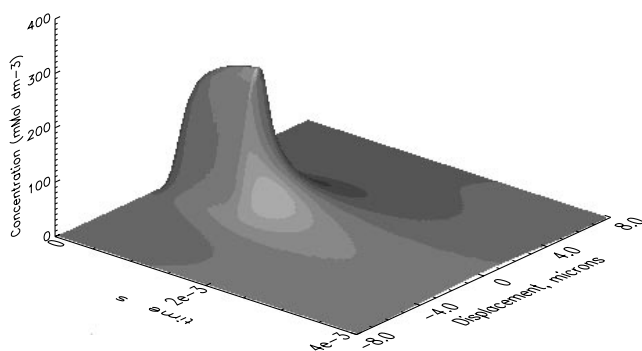


Fig. 10. Time-evolution of lateral profiles of H_2O_2 5 keV, dwelltime = 10^{-3} s.

that vary by 50 times over that in the 25 keV system over 1/15th of the distance. This enormous change in concentration gradient is responsible for the different effects of diffusion.

Diffusion can also be followed with the time-evolution of hydrogen peroxide. Figure 10 shows the characteristic broadening and flattening of the concentration profile as a result of diffusion. Here the dwelltime was 10^{-3} s. As we have already noted that annihilation is not too significant for H_2O_2 , this behaviour can be taken as evidence of diffusion.

Dominance of the hydroxyl radical

We now turn our attention to the individual species. The behaviour of $e_{(aq)}^-$, H^+ , $\text{H}^+_{(aq)}$ is straightforward. All are highly reactive, so the fact that they quickly reach a concentration where annihilation exceeds creation is not surprising (Figs 3, 4, 8(a) and (b)).

Hydrogen peroxide is not very reactive on this timescale (Table 2), so its high concentration and slow decay is entirely reasonable. Indeed, in the reaction scheme of Hill & Smith (1994), it only reacts with the hydrogen radical (reaction 7, Table 2). As it is also the product of $\cdot\text{OH}$ self-annihilation (reaction 1, Table 2), we expect to find H_2O_2 present in large quantities (Figs 3–7, 8(a), (b) and 9(a)).

More interesting is the hydroxyl radical, which has a similar behaviour, although it is far more reactive than hydrogen peroxide, and so would be expected to react away quickly. However $\cdot\text{OH}$ is produced in significant quantities (Table 3) and the routes of annihilation are limited by the low concentration of other species. Self-annihilation is possible but the rate is rather slow, at $0.45 \times 10^{10} \text{ M}^{-1} \text{ s}^{-1}$ (Eq. (1) in Table 2). This lack of annihilation routes means that $\cdot\text{OH}$ has a high concentration, and is expected to be the dominant damage-causing species. It is also relatively long-lived in water,

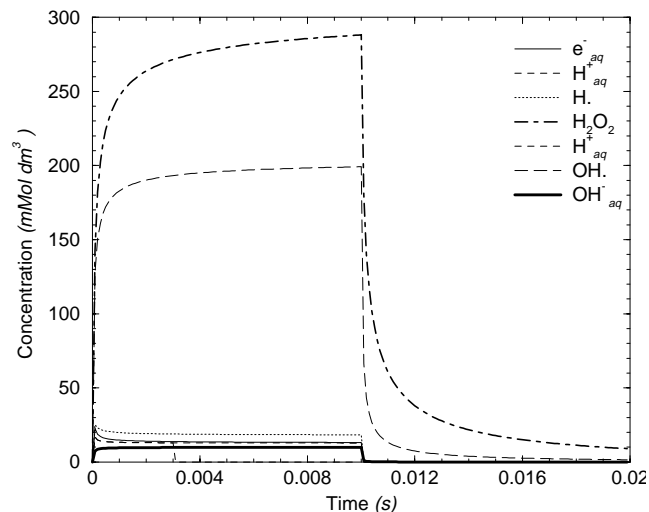


Fig. 11. After sufficient dwelltime, the central concentration tends towards a steady state (5 keV).

again from lack of annihilation routes, further increasing the potential for damage.

The approach to equilibrium

For longer dwelltimes, the system tends towards a steady state in the $r = 0$ region (Fig. 11). After the concentration peaks, annihilation is dominant, but in a regime of falling concentration rates of reaction are also reduced, so the concentrations tend towards an equilibrium value. Diffusion also becomes more and more significant for hydrogen peroxide and the hydroxyl radical by the time they have reached high concentration. Eventually, the competition between annihilation and diffusion, and radiolysis tends towards equilibrium, as shown in Fig. 11. The central concentrations are all largely constant after a dwelltime of 10^{-2} s for the 5 keV system.

The system as a whole does not approach equilibrium, as diffusion continues to spread the concentration profiles at all times. Additionally, far from the centre, we expect the concentrations to simply increase at all times, and not to exhibit clear maxima (Figs 5 and 10).

Conclusions

This simple first-order approach can determine the concentrations of reactive species in an ESEM water specimen. The environment is clearly hostile due to the presence of free radicals, which are not found to annihilate totally whilst receiving electrons from the primary beam. Increased radiation damage in the presence of water as found by Kitching & Donald (1998) and Jenkins & Donald (1997) is therefore not surprising.

The concentration of the hydroxyl radical suggests that this is the dominant mechanism for specimen degradation via free

radical attack. The high concentration of .OH appears to be due (i) to its high primary yield and (ii) to the shortage of decay routes available in the absence of other reactive species. Hydrogen peroxide is also present in large quantities, but is relatively stable on the timescales considered here. There is significant transport of the hydroxyl radical beyond the interaction volume for 5 keV PEs. Although diffusion is much reduced in the 25 keV system, much more of the specimen is damaged in any case, because of the longer PE range.

This longer PE range means that the reactive species are more widely spread in the 25 keV case. Although the concentration is increased by the fact that five times as many species are created due to the increase in absorbed energy, the vastly increased interaction volume still means that the reactive species have a much lower concentration than in the 5 keV case. This reduces annihilation, which is concentration dependent. The reactive species thus have longer lifetimes in the 25 keV system. Furthermore, due to the higher rate of annihilation with a lower beam energy, a lower beam energy and higher current should be significantly less damaging than a higher beam energy and lower current. Although these findings are hardly surprising, the significance lies in the ability to identify the dominant species and obtain a semi-quantitative estimate of the concentration profiles involved.

It is clear that radiation damage is much reduced with a lower beam energy, if the damage is due to absolute quantity of species, rather than local concentration. As already noted, dwelltimes are also longer in the case of 25 keV, as the beam takes longer to scan across the larger interaction volume. From this work, it is clear that the increase in radiation damage with beam energy is expected to be highly non-linear. Any reduction in beam energy during experimental work is therefore very desirable. Conversely, more work needs to be done in the area of X-ray microanalysis of hydrated species, where beam currents and dwelltimes used far exceed those for imaging.

The conclusions derived from this work lead us to speculate on possible approaches for reducing radiolysis damage. Of particular interest is the knowledge of the concentrations of various species such as peroxide, H^+ and OH^- . Armed with this information, it may be possible to load certain specimens with appropriate buffers or otherwise benign species that will preferentially scavenge the more damaging radiolysis products. Clearly much more work is needed in this area as electron microscopy of hydrated specimens becomes more commonplace.

References

- Danilatos, G.D. (1993) Introduction to the ESEM Instrument. *Microsc. Res. Techniq.* **25**, 354–361.
- Fletcher, A.L. (1998) Cryogenic developments and signal amplification in Environmental Scanning Electron Microscopy. PhD Thesis, Department of Physics, University of Cambridge, Cambridge.
- Goldstein, J.I., Newbury, D.E., Echlin, P., Joy, D.C., Romig, A.D. Jr, Lyman, C.E., Fiori, C. & Lifshin, E. (1992) *Scanning Electron Microscopy and X-Ray Microanalysis*, 2nd edn. Plenum Press, New York.
- Hill, M.A. & Smith, F.A. (1994) Calculation of initial and primary yields in the radiolysis of water. *Rad. Phys. Chem.* **43**, 265–280.
- Jenkins, L.M. & Donald, A.M. (1997) Use of the ESEM for the observation of the swelling behaviour of cellulosic fibres. *Scanning*, **19**, 92–97.
- Jonah, C.D., Matheson, M.S., Miller, J.R. & Hart, E.J. (1976) Yield and decay of the hydrated electron from 100 ps to 3 ns. *J. Phys. Chem.* **80**, 1267–1270.
- Jonah, C.D. & Miller, J.R. (1977) Yield and decay of the OH radical from 100 ps to 3 ns. *J. Phys. Chem.* **81**, 1974–1976.
- Kitching, S. & Donald, A.M. (1998) Beam damage of polypropylene in the environmental scanning electron microscope: an FTIR study. *J. Microsc.* **190**, 357–365.
- Kreyszig, E. (1993) *Advanced Engineering Mathematics*, 5th edn. Wiley, New York.
- La Verne, J.A. & Mozumder, A. (1983) Penetration of low-energy electrons in water. *Radiat. Res.* **96**, 219–234.
- Pimblott, S.M., LaVerne, J.M. & Mozumder, A. (1996) Monte Carlo simulation of range and energy deposition by electrons in gaseous and liquid water. *J. Phys. Chem.* **100**, 8595–8606.
- Pimblott, S.M., Pilling, M.J. & Green, N.J.B. (1991) Stochastic models of spur kinetics in water. *Radiat. Phys. Chem.* **37**, 377–388.
- Press, W.H., Teukolsky, S.A., Vetterling, W.T. & Flannery, B.P. (1988) *Numerical Recipes in C*, 2nd edn. Cambridge University Press, Cambridge.
- Reif, F. (1965) *Fundamentals of Statistical and Thermal Physics*. McGraw-Hill, New York.
- Talmon, Y. (1987) Electron beam radiation damage to organic and biological cryospecimens. *Cryotechniques in Biological Electron Microscopy*, (ed. by R. A. Steinbrecht and K. Zierold), pp. 64–84. Springer-Verlag, Berlin.
- Terrissol, M. & Beaudre, A. (1990) Simulation of space and time evolution of radiolytic species induced by electrons in water. *Radiat. Prot. Dosim.* **31**, 175–177.
- Thiel, B.L. & Donald, A.M. (1998) *In situ* mechanical testing of fully hydrated carrots (*Daucus carota*) in the environmental SEM. *Ann. Bot.* **82**, 727–733.

Appendix

The contribution from diffusion

We seek an expression for $D\nabla^2\Phi_\alpha(r,t)$, to satisfy the right-hand side of the diffusion equation (Eq. (11)) where we have the $\Phi_\alpha(r,t)$ discretely defined for a number of elements. In Cartesian co-ordinates,

$$\nabla^2\Phi_\alpha(r,t) = \frac{\partial}{\partial x^2}\Phi_\alpha(r,t) + \frac{\partial}{\partial y^2}\Phi_\alpha(r,t) + \frac{\partial}{\partial z^2}\Phi_\alpha(r,t). \quad (14)$$

The finite difference scheme considers the specimen as a number of cubic elements, of separation h along the x -axis. $\frac{\partial}{\partial x^2}\Phi_\alpha(r,t)$ for the n th element is found from the central difference theorem (Kreyszig, 1993; Press *et al.*, 1988),

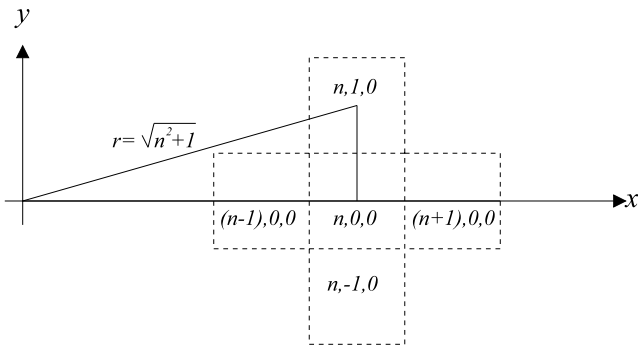


Fig. 12. Adjacent elements to the n th element along the x -axis. Approximate values of $\Phi_\alpha(r, t)$ are found for the elements above and below the x -axis by linear interpolation along the x -axis.

$$\frac{\partial}{\partial x^2} \Phi_\alpha(r, t) = \frac{1}{h^2} \{ \Phi_\alpha((n-1)h, 0, 0) - 2\Phi_\alpha(nh, 0, 0) + \Phi_\alpha((n+1)h, 0, 0) \}. \quad (15)$$

Boundary conditions are taken as a mirror at $r = 0$ through which no diffusion is permitted. For large r (typically $100 \mu\text{m}$) an equilibrium concentration is used. This is set to 10^{-7} M for $H^+_{(aq)}$ and $OH^-_{(aq)}$, and 10^{-42} M for other species. The values for $H^+_{(aq)}$ and $OH^-_{(aq)}$ are taken for pH 7. Other values take the equilibrium concentration of OH as a guide to typical values of reactive species. Considering cells adjacent to the x -axis (Fig. 12), the central difference method yields for the n th element along the x -axis,

$$\frac{\partial^2}{\partial y^2} \Phi_\alpha(r, t) \approx \frac{1}{h^2} \{ \Phi_\alpha(nh, -h, 0) - 2\Phi_\alpha(nh, 0, 0) + \Phi_\alpha(nh, h, 0) \}. \quad (16)$$

The values for $\Phi_\alpha(nh, \pm h, 0)$ are found from linear interpolation (Fig. 12) of $\Phi_\alpha((n-1)h, 0, 0)$ and $\Phi_\alpha((n+1)h, 0, 0)$ to give

$$\begin{aligned} \Phi_\alpha(nh, h, 0) \approx & \frac{1}{2h} \{ \Phi_\alpha((n+1)h, 0, 0) \\ & - \Phi_\alpha((n-1)h, 0, 0) \} \{ \sqrt{n^2 + 1} - n \} \\ & + \Phi_\alpha(nh, 0, 0). \end{aligned} \quad (17)$$

Substitution into Eq. (16) gives

$$\begin{aligned} \frac{\partial^2}{\partial y^2} \Phi_\alpha(nh, h, 0) \approx & \frac{1}{h^2} \{ \Phi_\alpha((n+1)h, 0, 0) \\ & - \Phi_\alpha((n-1)h, 0, 0) \} \{ \sqrt{n^2 + 1} - n \} \end{aligned} \quad (18)$$

Since from symmetry,

$$\frac{\partial^2}{\partial y^2} \Phi_\alpha(x, y, z) = \frac{\partial^2}{\partial z^2} \Phi_\alpha(x, y, z) \quad (19)$$

the contribution from diffusion is

$$\begin{aligned} \frac{\partial}{\partial t_{diff}} \Phi_\alpha(r, t) \approx & -\frac{D}{h^2} \{ \Phi_\alpha((n-1)h, 0, 0) - 2\Phi_\alpha(nh, 0, 0) \\ & + \Phi_\alpha((n+1)h, 0, 0) \} \\ & - 2\frac{D}{h^2} \{ \Phi_\alpha((n+1)h, 0, 0) \\ & - \Phi_\alpha((n-1)h, 0, 0) \} \{ \sqrt{n^2 + 1} - n \} \end{aligned} \quad (12)$$

For the case $n = 0$, the x , y and z components are all equal by symmetry, and all three axes are treated as a mirror. Although linear interpolation is only accurate to first order, it requires only one-dimensional arrays for the $\Phi_\alpha(r, t)$, allowing a smaller element size to be used.